Role of polarization-photon coupling in ultrafast terahertz excitation of ferroelectrics

Shihao Zhuang and Jia-Mian Hu

Phys. Rev. B **106**, L140302 — Published 18 October 2022

DOI: 10.1103/PhysRevB.106.L140302

Role of Polarization-Photon Coupling in Ultrafast Terahertz Excitation of Ferroelectrics

Shihao Zhuang and Jia-Mian Hu*
Department of Materials Science and Engineering, University of Wisconsin-Madison, Madison, WI, 53706, USA

Abstract

We investigate the role of polarization-photon coupling (specifically, polarization-oscillation-induced radiation electric field) in the excitation of ferroelectric thin films by an ultrafast terahertz (THz) electric-field pulse. Analytical formulae are developed to predict how the frequencies and relaxation time of three-dimensional soft mode phonons (intrinsic polarization oscillation) are modulated by radiation electric field and epitaxial strain. Ultrafast THz-pulse-driven excitation of harmonic polarization oscillation in strained single-domain ferroelectric thin film is then simulated using a dynamical phase-field model that considers the coupled strain-polarization-photon dynamics. The frequencies and relaxation time extracted from such numerical simulations agree well with analytical predictions. In relatively thin films, it is predicted that the radiation electric field slightly reduces the frequencies but significantly shortens the relaxation time. These results demonstrate the necessity of considering polarization-photon coupling in understanding and predicting the response of ferroelectric materials to ultrafast pulses of THz and higher frequencies.

*E-mail: jhu238@wisc.edu

Introduction. Ultrafast light-matter interaction is a promising route to understanding and controlling quantum materials where the four fundamental degrees of freedoms (charge, spin, orbit, and lattice) are dynamically intertwined [1,2]. By tailoring the wavelength, duration, and amplitude of ultrafast light pulse, one can probe the coupling among different quasiparticles (e.g., phonons, magnons), switch the material to a degenerate ground-state or a hidden metastable state of matter, or induce phase transitions [3,4]. Ferroelectric materials have a spontaneous polarization that can be switched by its conjugate electric field or other non-conjugate stimuli. Ultrafast light control of ferroelectrics offers potential for developing photoferroic devices with order of magnitude higher operation speed than those controlled by voltage [5]. In archetypal ferroelectric system such as $PbTiO_3$ and $BaTiO_3$, the development of the spontaneous polarization **P** is attributed to the condensation of a particular soft mode phonon A_1(TO) (see Fig. 1a) below the Curie temperature [6–8]. Depending on wavelength of the light pulse, ultrafast light control of polarization in ferroelectrics can occur through nonlinear coupling between the soft mode phonons and the near-infrared pluses via impulsive stimulated Raman Scattering [9,10], resonant coupling between the soft mode phonons and the terahertz (THz) pulse [11–19], indirect manipulation of soft mode phonons by mid-infrared pulses [20–25], and above-bandgap excitation [26–29].

Among these mechanisms, the use of THz electric-field pulse to drive soft mode phonon, whose resonant frequency is also in the THz range, is most straightforward [5]. Since the theoretical proposal for achieving picosecond (*ps*) polarization reversal by shaped THz electric-field pulses [11], ultrafast THz-field induced *ps* polarization dynamics has been experimentally observed in various ferroelectric materials systems [12,14–17,19]. Moreover, a recent experiment shows that applying a THz electric-field pulse can transiently drive the quantum paraelectric $SrTiO_3$ into a ferroelectric state [16]. Furthermore, molecular dynamics simulations predict that ultrafast THz electric-field excitation can induce hidden phase of polarization order in relaxor ferroelectric systems [18]. Despite these extensive works, the role of polarization-photon coupling, i.e., the emission of electromagnetic (EM) waves from the oscillating polarization and the backaction of the emitted EM waves on polarization dynamics, has not yet been addressed in existing atomistic [11,13,18] and mesoscale [19,30] simulations.

In this Letter, we formulate the frequencies and relaxation time of the three-dimensional (3D) soft mode phonon, which refers to the intrinsic oscillation of all three components P_x, P_y, P_z of the spontaneous polarization **P** [25], in the harmonic regime. Our analytical formulations are developed partly based on the work by Morozovska and colleagues [31], but here we consider the influences of polarization-oscillation-induced radiation electric field and epitaxial strain in ferroelectric thin films. Using an in-house dynamical phase-field model that considers coupled dynamics of strain, polarization, and EM waves, we then numerically simulate the excitation of harmonic polarization oscillation in a single-domain $(100)_{pc}$ $BaTiO_3$ thin film (pc: pseudocubic) by applying an ultrafast THz electric-field pulse of moderate amplitude. The values of frequencies and relaxation time extracted from numerical simulation results agree well with the analytical calculation. Our results demonstrate the necessity of considering radiation electric field in understanding and predicting ultrafast THz excitation of ferroelectrics.

Analytical Model. Let us consider a $(100)_{pc}$ $BaTiO_3$ film epitaxially grown on a $(110)_O$ $PrScO_3$ substrate (O: orthorhombic) as an example, as shown in Fig. 1a. In such a heterostructure, the combination of anisotropic lattice mismatch strain and interfacial symmetry breaking can stabilize an in-plane-polarized single ferroelectric domain in the $BaTiO_3$ film, which has been demonstrated experimentally [32]. Figure 1b shows the profile of the total free energy density (f^{tot}) of such

anisotropically strained $(100)_{pc}$ $BaTiO_3$ thin film at thermodynamic equilibrium, where P_y=0 and the anisotropy mismatch strain ε_{xx}^{mis} = 0.5%, ε_{yy}^{mis} = 0.01% and ε_{xy}^{mis} = 0 [32]. As shown, the equilibrium polarizations are located at the two degenerate energy minima at $\pm\mathbf{P}^0$, where $\mathbf{P}^0=(P_x^0, P_y^0, P_z^0)$ = (0.294, 0, 0) C m^{-2}. P_z is always 0 at equilibrium because of the depolarization field and because the anisotropic mismatch strain favors an in-plane polarization along the *x*-axis. An ultrafast external stimulus such as a THz pulse can perturb the polarization away from the $\mathbf{P}^0$. After then, the polarization will oscillate around the $\mathbf{P}^0$ at its intrinsic frequency until it returns to equilibrium via damping. The slope of the local free energy landscape represents the magnitude of the total effective electric field, $E_i^{eff} = -\frac{\partial f^{tot}}{\partial P_i}$ (i = x, y, z), that drives the polarization oscillation. In the harmonic regime (dashed line), E_i^{eff} is approximately proportional to the variation of polarization ΔP_i, as will be discussed shortly.

The frequency and relaxation time of the soft mode phonons in the harmonic regime can be analytically derived by linearizing the equation of anharmonic motion for the polarization [31,33,34], given as,

$$\mu\frac{\partial^2 P_i}{\partial t^2}+\gamma\frac{\partial P_i}{\partial t}=E_i^{eff} \quad (1)$$

where P_i are the three polarization components; μ and γ are the mass and damping coefficient, respectively. For a single-domain strained ferroelectric thin film, $E_i^{eff}=E_i^{Landau}+E_i^{elas}+E_i^{ext}+E_i^{d}$. Among them, $E_i^{Landau}=-\frac{\partial f^{Landau}}{\partial P_i}$ is the effective electric field from the Landau free energy density. Using an eighth-order Landau free energy density for $BaTiO_3$ [35], E_i^{Landau} is evaluated as,

$$E_i^{Landau}=-2\alpha_1 P_i-4\alpha_{11}P_i^3-2\alpha_{12}P_i\left(P_j^2+P_k^2\right)-6\alpha_{111}P_i^5-4\alpha_{112}P_i^3\left(P_j^2+P_k^2\right)-2\alpha_{112}P_i\left(P_j^4+P_k^4\right)-2\alpha_{123}P_iP_j^2P_k^2$$
$$-8\alpha_{1111}P_i^7-2\alpha_{1112}P_i\left[P_j^6+P_k^6+3P_i^4\left(P_j^2+P_k^2\right)\right]-4\alpha_{1122}P_i^3\left(P_j^4+P_k^4\right)-2\alpha_{1123}P_iP_j^2P_k^2(2P_i^2+P_j^2+P_k^2), \quad (2)$$

where $i = x, y, z$, and $j \neq i$, $k \neq i, j$; $\boldsymbol{\alpha}$ are Landau–Devonshire coefficients among which $\alpha_1=\alpha_0(T-T_c)$ is a linear function of temperature, and T_c is the Curie temperature. These coefficients are also provided in ref. [35]. The calculations and simulations in this work are all performed at T=298 K. The cubic and higher-order terms of $\mathbf{P}$ in Eq. (2) allow for modeling anharmonic polarization oscillation [12,34]. The expression of the elastic energy density f^{elas} is given in ref. [36] and the analytical expression of the corresponding effective field E_i^{elas} is derived in ref. [37].

The external electric field $\mathbf{E}^{ext}=\mathbf{E}^{app}+\mathbf{E}^{EM}$ is the sum of the applied electric field $\mathbf{E}^{app}$ and the radiation electric field $\mathbf{E}^{EM}$ in the ferroelectric thin film. $\mathbf{E}^{EM}$ describes the backaction of the emitted EM wave on polarization dynamics. For a film that has a uniform polarization and is infinitely large in the *xy* plane, $\mathbf{E}^{EM}$ propagates along the film thickness direction in the form of a plane wave with E_z^{EM}=0. The analytical expressions of E_x^{EM} and E_y^{EM} can be obtained by adapting the established procedures [38,39]. Specifically, our derivations [40] indicate that $E_i^{EM}(t) \approx -\frac{1}{2}\frac{d}{\kappa_0 c}\frac{\partial P_i}{\partial t}(t)$, i=x,y when the film thickness d is sufficiently small (c is the speed of light in vacuum), and this expression is equivalent to that used in ref. [12]. The depolarizing field $\mathbf{E}^d$ satisfies the Gauss's law $\nabla\cdot\mathbf{D} = \rho_f$, where $\mathbf{D}= \kappa_0\kappa_b\mathbf{E}^d+\mathbf{P}$ is electric displacement field; κ_0 and κ_b are the vacuum permittivity and background dielectric constant [41–43], respectively; ρ_f is the free charge density.

For a thin film with a spatially uniform **P**, an infinitely large *xy* plane, and $\rho_f = 0$, $\mathbf{E}^d$ can be solved analytically as $(E_x^d, E_y^d, E_z^d) = (0, 0, -\frac{P_z}{\kappa_0 \kappa_b})$.

With a knowledge of the analytical expressions of all the effective fields contributing to the E_i^{eff}, we now linearize Eq. (1) by assuming that $P_i = P_i^0 + \Delta P_i(t)$, where the $\Delta P_i(t) = \Delta P_i^0 e^{\mathbf{i}\omega_i t} e^{-\lambda_i t}$ takes the form of a damped harmonic oscillation; ω_i and ΔP_i^0 are the angular frequency and peak amplitude of the oscillation, respectively; λ_i is an auxiliary damping coefficient and the bold '**i**' refers to the imaginary unit. Based on these, Eq. (1) can be rewritten as,

$$\left(\mu\lambda_i^2 - \mu\omega_i^2 - \gamma\lambda_i\right)\Delta P_i(t) + \mathbf{i}(\gamma\omega_i - 2\omega_i\lambda_i\mu)\Delta P_i(t) = E_i^{eff}(\mathbf{P}^0) + \Delta E_i^{eff}(t), \quad (3)$$

where $E_i^{eff}(\mathbf{P}^0)$ refers to the total effective field at initial equilibrium state, and thus $E_i^{eff}(\mathbf{P}^0) = 0$; $\Delta E_i^{eff}(t) = \Delta E_i^d(t) + \Delta E_i^{EM}(t) + \Delta E_i^{Landau}(t) + \Delta E_i^{elas}(t)$ is the temporal variation of the E_i^{eff}. Based on the expression of $\mathbf{E}^d$ mentioned above, the variation of the depolarization field $\Delta\mathbf{E}^d(t) = (0, 0, -\frac{\Delta P_z}{\kappa_0 \kappa_b})$. Since there is no radiation electric field at the initial equilibrium state, $\Delta E_i^{EM}(t) = E_i^{EM}(t)$. Plugging in the expression of $\Delta P_i(t)$ into the analytically derived $E_i^{EM}(t)$ shown above, one has $E_i^{EM}(t) \approx -\frac{1}{2}\frac{d}{\kappa_0 c}(\mathbf{i}\omega_i - \lambda_i)\Delta P_i(t)$ (i = x, y). In the case of near-equilibrium (harmonic) excitation, one has $\Delta E_i^{Landau}(t) \approx A_i(\mathbf{P}^0)\Delta P_i(t) = \frac{\partial E_i^{Landau}}{\partial P_i}(\mathbf{P}^0)\Delta P_i(t)$ and $\Delta E_i^{elas}(t) \approx B_i(\mathbf{P}^0)\Delta P_i(t) = \frac{\partial E_i^{elas}}{\partial P_i}(\mathbf{P}^0)\Delta P_i(t)$ [44]. Taken together, Eq. (3) can be further written as,

$$\left(\mu\lambda_i^2 - \mu\omega_i^2 - \gamma\lambda_i\right) + \mathbf{i}\left(\gamma\omega_i - 2\omega_i\lambda_i\mu + \frac{1}{2}\frac{d}{\kappa_0 c}\omega_i\right) = A_i(\mathbf{P}^0) + B_i(\mathbf{P}^0) + \frac{1}{2}\frac{d}{\kappa_0 c}\lambda_i,\ i=x,y, \quad (4a)$$

$$\left(\mu\lambda_i^2 - \mu\omega_i^2 - \gamma\lambda_i\right) + \mathbf{i}(\gamma\omega_i - 2\omega_i\lambda_i\mu) = A_i(\mathbf{P}^0) + B_i(\mathbf{P}^0) - \frac{1}{\kappa_0 \kappa_b},\ i=z. \quad (4b)$$

Since the terms on the right-hand side of the Eqs. (4a-b) are all real numbers, the imaginary parts of the terms on the left-hand side must be equal to 0, from which the λ_i can be derived as,

$$\lambda_x = \lambda_y = \left(\gamma + \frac{1}{2}\frac{d}{\kappa_0 c}\right)/(2\mu)\ ;\ \lambda_z = \gamma/(2\mu) \quad (5)$$

As indicated by Eq. (5), the nonzero radiation electric field E_x^{EM} and E_y^{EM} induce a thickness(d)-dependent damping term for the oscillation of the in-plane polarization P_x and P_y. The oscillation of the out-of-plane polarization P_z, by comparison, is only subjected to the intrinsic damping because $E_z^{EM} = 0$. Plugging in the formulas of λ_i back to the Eqs. (4a-b), after some rearrangement, the angular frequencies of oscillation can be obtained as

$$\omega_i = \sqrt{-\frac{A_i + B_i}{\mu} - \lambda_i^2},\ i=x,y;\ \omega_i = \sqrt{-\frac{A_i + B_i - (1/\kappa_0\kappa_b)}{\mu} - \lambda_i^2},\ i=z. \quad (6)$$

Based on Eq. (6), we can calculate the intrinsic oscillation frequencies of polarization via $f_i = \omega_i/(2\pi)$. The relaxation time τ_i, which is the time for the peak amplitude of $\Delta P_i(t)$ to drop from its maximum to 1/e of that value, is calculated as $\tau_i = 1/\lambda_i$.

Figure 2a and 2b show the intrinsic frequency f_i and the relaxation time τ_i of the 3D soft mode phonon as a function of the film thickness d of the in-plane-polarized single-domain $(100)_{pc}$

$BaTiO_3$ film, respectively. For simplicity, we assume the film is always coherently strained [45] and maintains a single-domain state. As shown in Fig. 2a, f_x and f_y (the oscillation frequencies of P_x and P_y) differ significantly from each other in the $(100)_{pc}$ $BaTiO_3$ film due to the discrepancies in the slope of the local free energy landscape along P_x and P_y. Both the f_x and f_y decrease as the d increases due to the stronger radiation-field induced damping in thicker films. When d reaches a threshold value, f_x (f_y) reduces to zero, indicating that the polarization dynamics is critically damped. At even larger d, the polarization dynamics becomes overdamped. There is no polarization oscillation in the case of critically or overdamped dynamics.

Figure 2a also shows that the influence of $\mathbf{E}^{EM}$ on the soft mode phonon frequency is relatively weak in thin ferroelectric films. For example, in a 10-nm-thick $(100)_{pc}$ $BaTiO_3$ film, the $\mathbf{E}^{EM}$ reduces the f_x from 5.590 THz to 5.589 THz, and the f_y from 1.363 THz to 1.357 THz. However, the trend is reverse for the thickness dependence of the relaxation time. As shown in Fig. 2b, for the 10-nm-thick film, the relaxation time calculated in the presence of $\mathbf{E}^{EM}$ is only 1.3 ps, which is less than $1/10^{th}$ of the value (13.5 ps) calculated without $\mathbf{E}^{EM}$.

Dynamical phase-field simulations. In order to demonstrate the analytically predicted effects of the $\mathbf{E}^{EM}$ on both the frequency (Fig. 2a) and relaxation time (Fig. 2b) of the soft mode phonons, we performed dynamical phase-field simulations to model the excitation of harmonic polarization oscillation in anisotropically strained, single-domain $(100)_{pc}$ $BaTiO_3$ film by a low-amplitude ultrafast THz electric-field pulse. Compared to existing dynamical phase-field models that only consider coupled polarization and strain dynamics [33,46], our model considers the coupled dynamics of strain, polarization, and EM waves by solving the nonlinear equations of motions for the polarization $\mathbf{P}$ (Eq. 1), the mechanical displacement $\mathbf{u}$, and the radiation electric field $\mathbf{E}^{EM}$ in a coupled fashion. Here, all different effective electric fields that contributes to the E_i^{eff}, including E_i^{Landau}, E_i^{elas}, E_i^{d}, E_i^{grad}, and the E_i^{EM}, are evaluated numerically without making approximations, which is different from the analytical model described in the previous section. Specifically, the E_i^{grad} results from the gradient energy density $f^{grad}=\frac{1}{2}G_{11}(\nabla\mathbf{P})^2$ and is calculated as $-\frac{\delta f^{grad}}{\delta P_i}=G_{11}\nabla^2 P_i$, where G_{11} is the isotropic gradient energy coefficient. Furthermore, the spatiotemporal distribution of the $\mathbf{E}^{EM}$ and associated radiation magnetic field $\mathbf{H}^{EM}$ are numerically obtained by solving the Maxwell's equations,

$$\frac{\partial \mathbf{E}^{EM}}{\partial t}=\frac{1}{\kappa_0\kappa_b}(\nabla\times\mathbf{H}^{EM}-\frac{\partial \mathbf{P}}{\partial t});\ \frac{\partial \mathbf{H}^{EM}}{\partial t}=-\frac{1}{\mu_0}\nabla\times\mathbf{E}^{EM}, \tag{7}$$

where the term $\frac{\partial \mathbf{P}}{\partial t}$ showing the time-varying polarization is the source of electric dipole radiation. The polarization and strain dynamics are coupled since the elastic effective electric field $\mathbf{E}^{elas}$ is a function of the polarization $\mathbf{P}$, stress-free strain $\boldsymbol{\varepsilon}^0$, and total strain $\boldsymbol{\varepsilon}$ [37]. Here, the total strain $\boldsymbol{\varepsilon}=\boldsymbol{\varepsilon}(\mathbf{P}^0)+\Delta\boldsymbol{\varepsilon}(t)$. The expression of the $\boldsymbol{\varepsilon}(\mathbf{P}^0)$, that is, the strain at the initial equilibrium state, is obtained by solving the mechanical equilibrium equation [47] and given in [37]. The $\Delta\boldsymbol{\varepsilon}(t)$ is calculated as $\Delta\varepsilon_{ij}=\frac{1}{2}\left(\frac{\partial\Delta u_i}{\partial j}+\frac{\partial\Delta u_j}{\partial i}\right)$, where $\Delta\,\mathbf{u}\,(t)$ is the temporal variation of the mechanical displacement $\mathbf{u}$ with $i, j = x, y, z$, and obtained by solving the elastodynamics equation for the entire film-on-substrate heterostructure,

$$\rho\frac{\partial^2\Delta\mathbf{u}}{\partial t^2}=\nabla\cdot[\mathbf{c}(\Delta\boldsymbol{\varepsilon}-\Delta\boldsymbol{\varepsilon}^0)] \tag{8}$$

where ρ and $\mathbf{c}$ are phase-dependent mass density and elastic stiffness tensor, respectively; $\Delta\boldsymbol{\varepsilon}^0(t) = \boldsymbol{\varepsilon}^0(t)-\boldsymbol{\varepsilon}^0(\mathbf{P}^0)$ is the temporal variation of the stress-free strain. Free surface mechanical boundary condition $\sigma_{iz}=0$ ($i = x, y, z$) is applied on the top surface of the ferroelectric film during the dynamics. The entire heterostructure is discretized into one-dimensional (1D) computational cells along z axis with a cell size of 1 nm. The $(110)_O$ $PrScO_3$ substrate and the free space above the ferroelectric film are discretized into 100 and 10 cells, respectively. When solving the Maxwell's equations, the absorbing boundary condition, expressed as $\frac{\partial \mathbf{E}^{EM}}{\partial z}=-\frac{1}{c}\frac{\partial \mathbf{E}^{EM}}{\partial t}$ [48], is applied on both the bottom and top surfaces of the computational system to prevent the reflection of the emitted EM waves back to the system. Likewise, the absorbing boundary condition for the mechanical displacement $\mathbf{u}$, $\frac{\partial u_i}{\partial z}=-\frac{1}{v}\frac{\partial u_i}{\partial t}$ (i=x,y,z) is applied at the bottom surface of the substrate to make the substrate a perfect sink for elastic waves, where v is the transverse sound velocity for u_x and u_y and the longitudinal sound velocity for u_z. Central finite difference is used to calculate spatial derivatives in all dynamical equations (Eqs. 1, 7 and 8), which are solved in a coupled manner using the classical Runge-Kutta method for time marching with a time step of 10^{-18} s. Specifically, the Maxwell's equations are solved using the finite-difference time-domain (FDTD) method. The validation of our in-house 1D FDTD solver is provided in our recent work [49]. Relevant materials parameters for the single-domain $BaTiO_3$ film and $PrScO_3$ substrate [50] are collected from refs. [19,31,35,51–54]. Moreover, our in-house numerical solvers for all equations are Graphics Processing Unit (GPU)-accelerated.

The THz electric-field pulse $\mathbf{E}^{app}(t)$ is applied along the y axis. The waveform of $\mathbf{E}^{app}(t)$, as shown in Fig. 3a, takes the form $E_y^{app}(t)=E_0^{app}\exp\left[-\frac{(t-t_0)^2}{w^2}\right]\cos[\omega^{app}(t-t_0)]$ based on [18]. Here $\omega^{app}/(2\pi)$ =1.5 THz defines the peak frequency of the THz electric-field pulse. E_0^{app} = 10^6 V m^{-1} and t_0 = 0.6 ps are the amplitude and temporal position of the peak electric field, respectively, while w = 0.2 ps is the width of the Gaussian function. At the initial equilibrium state, the polarization in the 10-nm-thick single-domain $(100)_{pc}$ $BaTiO_3$ film is along the +x-axis. Once a nonzero P_y is induced by E_y^{app}, a nonzero $\Delta P_x(t)=[P_x(t)-P_x^0]$ will be developed due to a nonzero but much smaller effective electric field E_x^{Landau} (see Eq. 2). As a result, both the E_y^{EM} and E_x^{EM} are nonzero, but the amplitude of the E_y^{EM} is two orders of magnitude larger, as shown in Fig. 3a and 3b. One can also apply the THz electric-field pulse along the in-plane diagonal axis, in which case P_x and P_y can be directly excited by the nonzero E_x^{app} and E_y^{app}, respectively. To excite harmonic polarization oscillation, the E_0^{app} cannot be too large, and meanwhile, the frequency window of the applied electric-field pulse needs to contain the frequencies of the soft mode phonons. For example, under the application of a gigahertz (GHz) electric field pulse, $\Delta\mathbf{P}$ would not oscillate after the $\mathbf{E}^{app}(t)$ is turned off [55]. In addition, the radiation electric field is negligible compared to the $\mathbf{E}^{app}(t)$ for GHz excitation due to the slower temporal variation of $\Delta\mathbf{P}$.

Figure 3c shows the evolution of the $\Delta P_y(t)$ in a 10-nm-thick $(100)_{pc}$ $BaTiO_3$ film with and without considering its conjugate radiation electric field component E_y^{EM}. Note that $\Delta P_y(t)=P_y(t)$ since P_y^0=0. As shown, the P_y reaches its peak amplitude at ~1.1 ps and decreases monotonically due to the damping. According to the analytical prediction, the E_y^{EM} reduces the intrinsic oscillation frequency of P_y from 1.363 THz to 1.357 THz (Fig. 2a) and the relaxation time from 13.5 ps to 1.3 ps (Fig. 2b). The reduced relaxation time can be clearly seen from Fig. 3c. Notably, the decrease in the peak values of ΔP_y at each oscillation period can be well described by the

analytical expression $|\Delta P_y|(t)=|\Delta P_y^0|e^{-\frac{(t-t^0)}{\tau}}$, where τ is the analytically calculated relaxation time (13.5 ps or 1.3 ps) and $\Delta P_y^0=P_y(t=t^0)$ is the peak amplitude as indicated in Fig. 3c with t^0 = 1.1 ps. The analytically calculated decreasing trajectories are shown as the dashed lines, which agree well with the simulation results. Figure 3d shows the frequency spectra of the simulated $\Delta P_y(t)$ curves with and without E_y^{EM} (see red and black curves). Both curves show a single peak at the 1.36 THz, which is consistent with the analytical prediction. The predicted frequency shift from 1.363 THz to 1.357 THz is too small to resolve numerically. However, our simulations using thicker $BaTiO_3$ film confirm the analytically predicted frequency shift as well as the absence of polarization oscillation in overdamped systems [56]. The frequency spectrum of the $E_y^{EM}(t)$ is also plotted in Fig. 3d, which displays a single peak at 1.36 THz, the same as that of $\Delta P_y(t)$. Moreover, the oscillation frequency of P_x extracted from the numerically simulated $\Delta P_x(t)$ is 5.6 THz [57], which is also consistent with the analytical calculation (see Fig. 2a). It is noteworthy that both the E_x^{EM} and E_y^{EM} have a sufficiently large amplitude in the time-domain (Figs. 3a-b). Specifically, the peak amplitude of the E_y^{EM} is nearly $1/5^{th}$ of the applied THz pulse E_y^{app}. Therefore, the predicted THz-pulse-induced polarization oscillation can in principle be experimentally characterized by THz-pump THz-probe spectroscopy, through which both the soft mode phonon frequencies and relaxation time can be experimentally determined. Furthermore, our simulations show that the radiation electric field can significantly modulate the frequency and the relaxation time of soft mode phonons in the anharmonic regime, which can be reached via intense THz excitation [12,58].

In conclusion, our results show that an accurate modeling of ultrafast THz-field excitation of ferroelectrics requires considering the polarization-dynamics-induced radiation electric field. Using ultrafast THz-field-induced harmonic polarization oscillation in single-domain ferroelectric thin film as an example, we analytically and numerically demonstrate that the radiation electric field can reduce the frequency and particularly the relaxation time of soft mode phonons by increasing the damping. We have derived the analytical expressions on the soft mode phonon frequencies as a function of epitaxial strain and thin film thickness, which can be utilized to guide the thin-film synthesis and the THz pulse engineering for achieving resonant THz excitation. Our GPU-accelerated dynamical phase-field model, which considers fully coupled dynamics of strain, polarization, and EM waves, can be extended to model polarization dynamics in more complex ferroelectric materials under the excitation by other types of ultrafast light pulses.

Acknowledgements. We are grateful for the helpful discussion with Haidan Wen. J.-M.H. acknowledges support from the NSF award CBET-2006028 and the Accelerator Program from the Wisconsin Alumni Research Foundation. The simulations were performed using Bridges at the Pittsburgh Supercomputing Center through allocation TG-DMR180076, which is part of the Extreme Science and Engineering Discovery Environment (XSEDE) and supported by NSF grant ACI-1548562.

References

[1] Y. Tokura, M. Kawasaki, and N. Nagaosa, *Emergent Functions of Quantum Materials*, Nat. Phys. **13**, 1056 (2017).

[2] B. Keimer and J. E. Moore, *The Physics of Quantum Materials*, Nat. Phys. **13**, 1045 (2017).

[3] A. Kirilyuk, A. V Kimel, and T. Rasing, *Ultrafast Optical Manipulation of Magnetic Order*, Rev. Mod. Phys. **82**, 2731 (2010).

[4] A. de la Torre, D. M. Kennes, M. Claassen, S. Gerber, J. W. McIver, and M. A. Sentef, *Colloquium: Nonthermal Pathways to Ultrafast Control in Quantum Materials*, Rev. Mod. Phys. **93**, 41002 (2021).

[5] A. V Kimel, A. M. Kalashnikova, A. Pogrebna, and A. K. Zvezdin, *Fundamentals and Perspectives of Ultrafast Photoferroic Recording*, Phys. Rep. **852**, 1 (2020).

[6] G. Burns and B. A. Scott, *Lattice Modes in Ferroelectric Perovskites: $PbTiO_3$*, Phys. Rev. B **7**, 3088 (1973).

[7] W. Zhong, D. Vanderbilt, and K. M. Rabe, *Phase Transitions in $BaTiO_3$ from First Principles*, Phys. Rev. Lett. **73**, 1861 (1994).

[8] C. M. Foster, M. Grimsditch, Z. Li, and V. G. Karpov, *Raman Line Shapes of Anharmonic Phonons*, Phys. Rev. Lett. **71**, 1258 (1993).

[9] Y. Yan and K. A. Nelson, *Impulsive Stimulated Light Scattering. I. General Theory*, J. Chem. Phys. **87**, 6240 (1987).

[10] S. Fahy and R. Merlin, *Reversal of Ferroelectric Domains by Ultrashort Optical Pulses*, Phys. Rev. Lett. **73**, 1122 (1994).

[11] T. Qi, Y.-H. Shin, K.-L. Yeh, K. A. Nelson, and A. M. Rappe, *Collective Coherent Control: Synchronization of Polarization in Ferroelectric $PbTiO_3$ by Shaped THz Fields*, Phys. Rev. Lett. **102**, 247603 (2009).

[12] I. Katayama, H. Aoki, J. Takeda, H. Shimosato, M. Ashida, R. Kinjo, I. Kawayama, M. Tonouchi, M. Nagai, and K. Tanaka, *Ferroelectric Soft Mode in a $SrTiO_3$ Thin Film Impulsively Driven to the Anharmonic Regime Using Intense Picosecond Terahertz Pulses*, Phys. Rev. Lett. **108**, 97401 (2012).

[13] R. Herchig, K. Schultz, K. McCash, and I. Ponomareva, *Terahertz Sensing Using Ferroelectric Nanowires*, Nanotechnology **24**, 45501 (2013).

[14] S. Grübel, J. A. Johnson, P. Beaud, C. Dornes, A. Ferrer, V. Haborets, L. Huber, T. Huber, A. Kohutych, and T. Kubacka, *Ultrafast X-Ray Diffraction of a Ferroelectric Soft Mode Driven by Broadband Terahertz Pulses*, ArXiv Prepr. ArXiv1602.05435 (2016).

[15] F. Chen, Y. Zhu, S. Liu, Y. Qi, H. Y. Hwang, N. C. Brandt, J. Lu, F. Quirin, H. Enquist, P. Zalden, T. Hu, J. Goodfellow, M.-J. Sher, M. C. Hoffmann, D. Zhu, H. Lemke, J. Glownia, M. Chollet, A. R. Damodaran, J. Park, Z. Cai, I. W. Jung, M. J. Highland, D. A. Walko, J. W. Freeland, P. G. Evans, A. Vailionis, J. Larsson, K. A. Nelson, A. M. Rappe, K. Sokolowski-Tinten, L. W. Martin, H. Wen, and A. M. Lindenberg, *Ultrafast Terahertz-Field-Driven Ionic Response in Ferroelectric $BaTiO_3$*, Phys. Rev. B **94**, 180104 (2016).

[16] L. Xian, Q. Tian, Z. Jiahao, B. Edoardo, L. Jian, R. A. M., and N. K. A., *Terahertz Field–Induced Ferroelectricity in Quantum Paraelectric $SrTiO_3$*, Science (80-.). **364**, 1079 (2019).

[17] V. Bilyk, E. Mishina, N. Sherstyuk, A. Bush, A. Ovchinnikov, and M. Agranat, *Transient Polarization Reversal Using an Intense THz Pulse in Silicon-Doped Lead Germanate*, Phys. Status Solidi – Rapid Res. Lett. **15**, 2000460 (2021).

[18] S. Prosandeev, J. Grollier, D. Talbayev, B. Dkhil, and L. Bellaiche, *Ultrafast Neuromorphic Dynamics Using Hidden Phases in the Prototype of Relaxor Ferroelectrics*, Phys. Rev. Lett. **126**, 27602 (2021).

[19] Q. Li, V. A. Stoica, M. Paściak, Y. Zhu, Y. Yuan, T. Yang, M. R. McCarter, S. Das, A. K. Yadav, S. Park, C. Dai, H. J. Lee, Y. Ahn, S. D. Marks, S. Yu, C. Kadlec, T. Sato, M. C. Hoffmann, M. Chollet, M. E. Kozina, S. Nelson, D. Zhu, D. A. Walko, A. M. Lindenberg, P. G. Evans, L.-Q. Chen, R. Ramesh, L. W. Martin, V. Gopalan, J. W. Freeland, J. Hlinka, and H. Wen, *Subterahertz Collective Dynamics of Polar Vortices*, Nature **592**, 376 (2021).

[20] A. Subedi, *Proposal for Ultrafast Switching of Ferroelectrics Using Midinfrared Pulses*, Phys. Rev. B **92**, 214303 (2015).

[21] R. Mankowsky, A. von Hoegen, M. Först, and A. Cavalleri, *Ultrafast Reversal of the Ferroelectric Polarization*, Phys. Rev. Lett. **118**, 197601 (2017).

[22] A. von Hoegen, R. Mankowsky, M. Fechner, M. Först, and A. Cavalleri, *Probing the Interatomic Potential of Solids with Strong-Field Nonlinear Phononics*, Nature **555**, 79 (2018).

[23] T. F. Nova, A. S. Disa, M. Fechner, and A. Cavalleri, *Metastable Ferroelectricity in Optically Strained $SrTiO_3$*, Science (80-.). **364**, 1075 (2019).

[24] M. Henstridge, M. Först, E. Rowe, M. Fechner, and A. Cavalleri, *Nonlocal Nonlinear Phononics*, Nat. Phys. (2022).

[25] P. Chen, C. Paillard, H. J. Zhao, J. Íñiguez, and L. Bellaiche, *Deterministic Control of Ferroelectric Polarization by Ultrafast Laser Pulses*, Nat. Commun. **13**, 2566 (2022).

[26] D. Daranciang, M. J. Highland, H. Wen, S. M. Young, N. C. Brandt, H. Y. Hwang, M. Vattilana, M. Nicoul, F. Quirin, J. Goodfellow, T. Qi, I. Grinberg, D. M. Fritz, M. Cammarata, D. Zhu, H. T. Lemke, D. A. Walko, E. M. Dufresne, Y. Li, J. Larsson, D. A. Reis, K. Sokolowski-Tinten, K. A. Nelson, A. M. Rappe, P. H. Fuoss, G. B. Stephenson, and A. M. Lindenberg, *Ultrafast Photovoltaic Response in Ferroelectric Nanolayers*, Phys. Rev. Lett. **108**, 87601 (2012).

[27] D. Schick, M. Herzog, H. Wen, P. Chen, C. Adamo, P. Gaal, D. G. Schlom, P. G. Evans, Y. Li, and M. Bargheer, *Localized Excited Charge Carriers Generate Ultrafast Inhomogeneous Strain in the Multiferroic $BiFeO_3$*, Phys. Rev. Lett. **112**, 97602 (2014).

[28] H. J. Lee, Y. Ahn, S. D. Marks, E. C. Landahl, S. Zhuang, M. H. Yusuf, M. Dawber, J. Y. Lee, T. Y. Kim, S. Unithrattil, S. H. Chun, S. Kim, I. Eom, S.-Y. Park, K. S. Kim, S. Lee, J. Y. Jo, J. Hu, and P. G. Evans, *Structural Evidence for Ultrafast Polarization Rotation in Ferroelectric/Dielectric Superlattice Nanodomains*, Phys. Rev. X **11**, 31031 (2021).

[29] V. A. Stoica, N. Laanait, C. Dai, Z. Hong, Y. Yuan, Z. Zhang, S. Lei, M. R. McCarter, A.

Yadav, A. R. Damodaran, S. Das, G. A. Stone, J. Karapetrova, D. A. Walko, X. Zhang, L. W. Martin, R. Ramesh, L.-Q. Chen, H. Wen, V. Gopalan, and J. W. Freeland, *Optical Creation of a Supercrystal with Three-Dimensional Nanoscale Periodicity*, Nat. Mater. **18**, 377 (2019).

[30] T. Yang, C. Dai, Q. Li, H. Wen, and L.-Q. Chen, *Condensation of Collective Polar Vortex Modes*, Phys. Rev. B **103**, L220303 (2021).

[31] A. N. Morozovska, Y. M. Vysochanskii, O. V Varenyk, M. V Silibin, S. V Kalinin, and E. A. Eliseev, *Flexocoupling Impact on the Generalized Susceptibility and Soft Phonon Modes in the Ordered Phase of Ferroics*, Phys. Rev. B **92**, 94308 (2015).

[32] J. W. Lee, K. Eom, T. R. Paudel, B. Wang, H. Lu, H. X. Huyan, S. Lindemann, S. Ryu, H. Lee, T. H. Kim, Y. Yuan, J. A. Zorn, S. Lei, W. P. Gao, T. Tybell, V. Gopalan, X. Q. Pan, A. Gruverman, L. Q. Chen, E. Y. Tsymbal, and C. B. Eom, *In-Plane Quasi-Single-Domain $BaTiO_3$ via Interfacial Symmetry Engineering*, Nat. Commun. **12**, 6784 (2021).

[33] T. Yang, B. Wang, J.-M. Hu, and L.-Q. Chen, *Domain Dynamics under Ultrafast Electric-Field Pulses*, Phys. Rev. Lett. **124**, 107601 (2020).

[34] V. L. Ginzburg, *Phase Transitions in Ferroelectrics: Some Historical Remarks*, Physics-Uspekhi **44**, 1037 (2001).

[35] Y. L. Li, L. E. Cross, and L. Q. Chen, *A Phenomenological Thermodynamic Potential for $BaTiO_3$ Single Crystals*, J. Appl. Phys. **98**, 64101 (2005).

[36] Y. L. Li, S. Y. Hu, Z. K. Liu, and L. Q. Chen, *Effect of Substrate Constraint on the Stability and Evolution of Ferroelectric Domain Structures in Thin Films*, Acta Mater. **50**, 395 (2002).

[37] See Supplemental Material at [URL] for the derivation of analytical expression of the $\mathbf{E}^{\text{elas}}$ for strained single-domain ferroelectric thin films.

[38] G. L. Pollack and D. R. Stump, *Electromagnetism* (American Association of Physics Teachers, 2005).

[39] B. U. Felderhof and G. Marowsky, *Electromagnetic Radiation from a Polarization Sheet Located at an Interface between Two Media*, Appl. Phys. B **44**, 11 (1987).

[40] See Supplemental Material at [URL] for the derivation of the analytical expression of the $\mathbf{E}^{\text{EM}}$ for single-domain ferroelectric thin films.

[41] A. K. Tagantsev, *The Role of the Background Dielectric Susceptibility in Uniaxial Ferroelectrics*, Ferroelectrics **69**, 321 (1986).

[42] A. K. Tagantsev, *Landau Expansion for Ferroelectrics: Which Variable to Use?*, Ferroelectrics **375**, 19 (2008).

[43] A. P. Levanyuk, B. A. Strukov, and A. Cano, *Background Dielectric Permittivity: Material Constant or Fitting Parameter?*, Ferroelectrics **503**, 94 (2016).

[44] See Supplemental Material at [URL] for the derivation of the analytical expressions of the $\Delta\mathbf{E}^{\text{Landau}}$ and $\Delta\mathbf{E}^{\text{elas}}$.

[45] See Supplemental Material at [URL] for the influence of mismatch strain on the frequency of soft mode phonon. The mismatch strain does not influence the relaxation time.

[46] T. Yang and L.-Q. Chen, *Dynamical Phase-Field Model of Coupled Electronic and Structural Processes*, Npj Comput. Mater. **8**, 130 (2022).

[47] L.-Q. Chen, *Phase-Field Method of Phase Transitions/Domain Structures in Ferroelectric Thin Films: A Review*, J. Am. Ceram. Soc. **91**, 1835 (2008).

[48] J.-M. Jin, *Theory and Computation of Electromagnetic Fields* (John Wiley & Sons, 2011).

[49] S. Zhuang and J.-M. Hu, *Excitation and Detection of Coherent Sub-Terahertz Magnons in Ferromagnetic and Antiferromagnetic Heterostructures*, Npj Comput. Mater. **8**, 167 (2022).

[50] See Supplemental Material at [URL] for the list of materials parameters used in dynamical phase-field simulations.

[51] Y. L. Li and L. Q. Chen, *Temperature-Strain Phase Diagram for $BaTiO_3$ Thin Films*, Appl. Phys. Lett. **88**, 72905 (2006).

[52] P. Tang, R. Iguchi, K. Uchida, and G. E. W. Bauer, *Excitations of the Ferroelectric Order*, Phys. Rev. B **106**, L081105 (2022).

[53] J. Hlinka and P. Márton, *Phenomenological Model of a 90^o Domain Wall in $BaTiO_3$-Type Ferroelectrics*, Phys. Rev. B **74**, 104104 (2006).

[54] A. K. Tagantsev and G. Gerra, *Interface-Induced Phenomena in Polarization Response of Ferroelectric Thin Films*, J. Appl. Phys. **100**, 51607 (2006).

[55] See Supplemental Material at [URL] for the control simulation under a GHz electric field pulse.

[56] See Supplemental Material at [URL] for the control simulations for 50-nm-thick and 150-nm-thick (100) $BaTiO_3$ films.

[57] See Supplemental Material at [URL] for the analyses of the numerically simulated $\Delta P_x(t)$.

[58] See Supplemental Material at [URL] for the control simulation under an intense THz electric-field pulse.

Figure Captions

Figure 1. (**a**) Schematics of the soft mode phonon A_1(TO) in $BaTiO_3$ (left), the excitation of the 3D soft mode phonon in a $BaTiO_3$(film)/$PrScO_3$(substrate) heterostructure by an ultrafast THz electric-field pulse $\mathbf{E}^{app}$, and the radiation electric field $\mathbf{E}^{EM}$ generated by the oscillating polarization **P**. The double-headed arrows indicate the polarization axis of the $\mathbf{E}^{app}$ or $\mathbf{E}^{EM}$. **(b)** Profile of the relative total free energy density (Δf^{tot}) of the anisotropically strained single-domain $(100)_{pc}$ $BaTiO_3$ film as a function of the P_x for P_y=0, where the dashed line indicates a harmonic fitting.

Figure 2. (a) Analytically calculated f_x and f_y (intrinsic oscillation frequency of P_x and P_y) as a function of the $(100)_{pc}$ $BaTiO_3$ film thickness d, with (solid lines) and without (dashed lines) considering the $\mathbf{E}^{EM}$. The enlarged f_y-d curves from d = 5 nm to 15 nm are shown in the inset. **(b)** Analytically calculated relaxation time τ of P_x and P_y oscillation as a function of d, with (solid line) and without (dashed line) considering the $\mathbf{E}^{EM}$. The enlarged τ-d curves from d=5 nm to 15 nm are shown in the inset.

Figure 3. Temporal profiles of the **(a)** $E_y^{EM}(t)$ and **(b)** $E_x^{EM}(t)$ at 2 nm above the 10-nm-thick $(100)_{pc}$ $BaTiO_3$ film upon the excitation by a THz electric-field pulse $\mathbf{E}^{app}(t)$, which is applied along the y-axis and shown by the right axis. The results are from dynamical phase-field simulations. Oscillation trajectories of **(c)** the $\Delta P_y(t)$ with (red solid line) and without (black solid line) considering the conjugate E_y^{EM}, obtained from dynamical phase-field (PF) simulations. The analytically calculated attenuation of the peak values of ΔP_y are plotted using the dashed lines. **(d)** Frequency spectra of the $E_y^{EM}(t)$ and the two solid lines of $\Delta P_y(t)$ in (c).

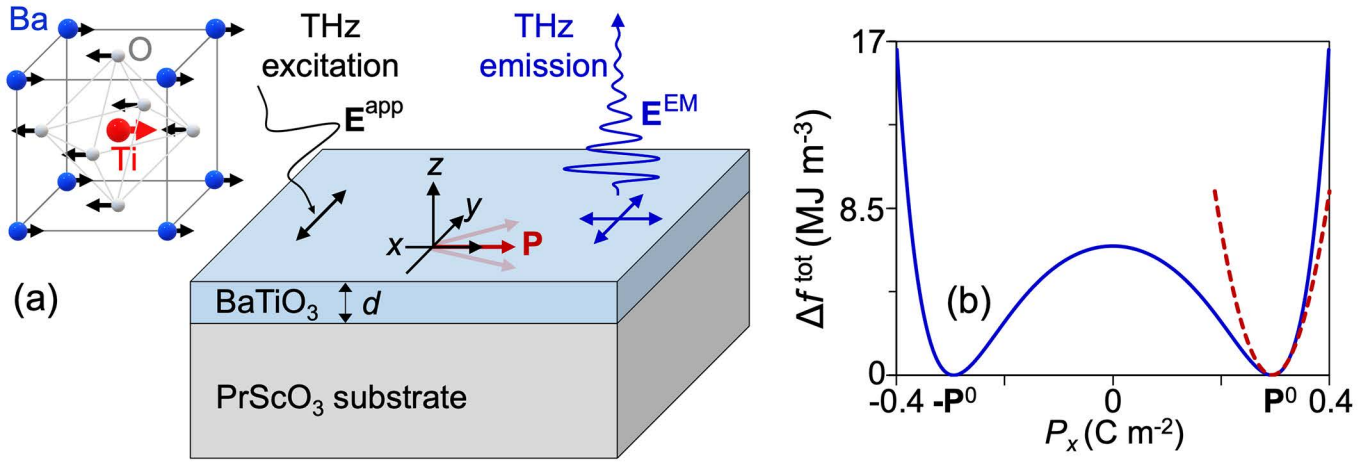
Ba
O
Ti
THz
excitation
THz
emission
E^app
E^EM
z
y
x
P
(a)
BaTiO3
d
PrScO3 substrate
17
8.5
0
Δf tot (MJ m-3)
(b)
-0.4
-P0
0
P0
0.4
Px (C m-2)

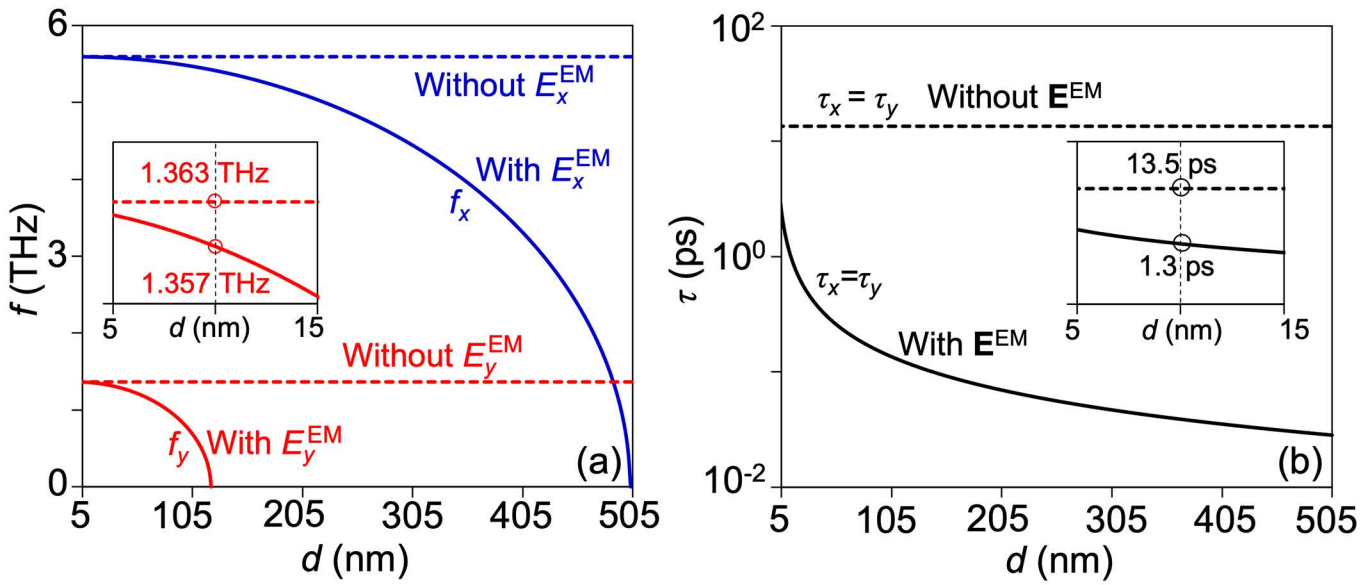
6
3
0
f (THz)
Without E_x^{EM}
With E_x^{EM}
f_x
1.363 THz
1.357 THz
5
d (nm)
15
Without E_y^{EM}
f_y
With E_y^{EM}
(a)
5
105
205
305
405
505
d (nm)
10^2
10^0
10^{-2}
τ (ps)
$\tau_x = \tau_y$
Without $\mathbf{E}^{EM}$
13.5 ps
1.3 ps
τ_x=τ_y
With $\mathbf{E}^{EM}$
(b)

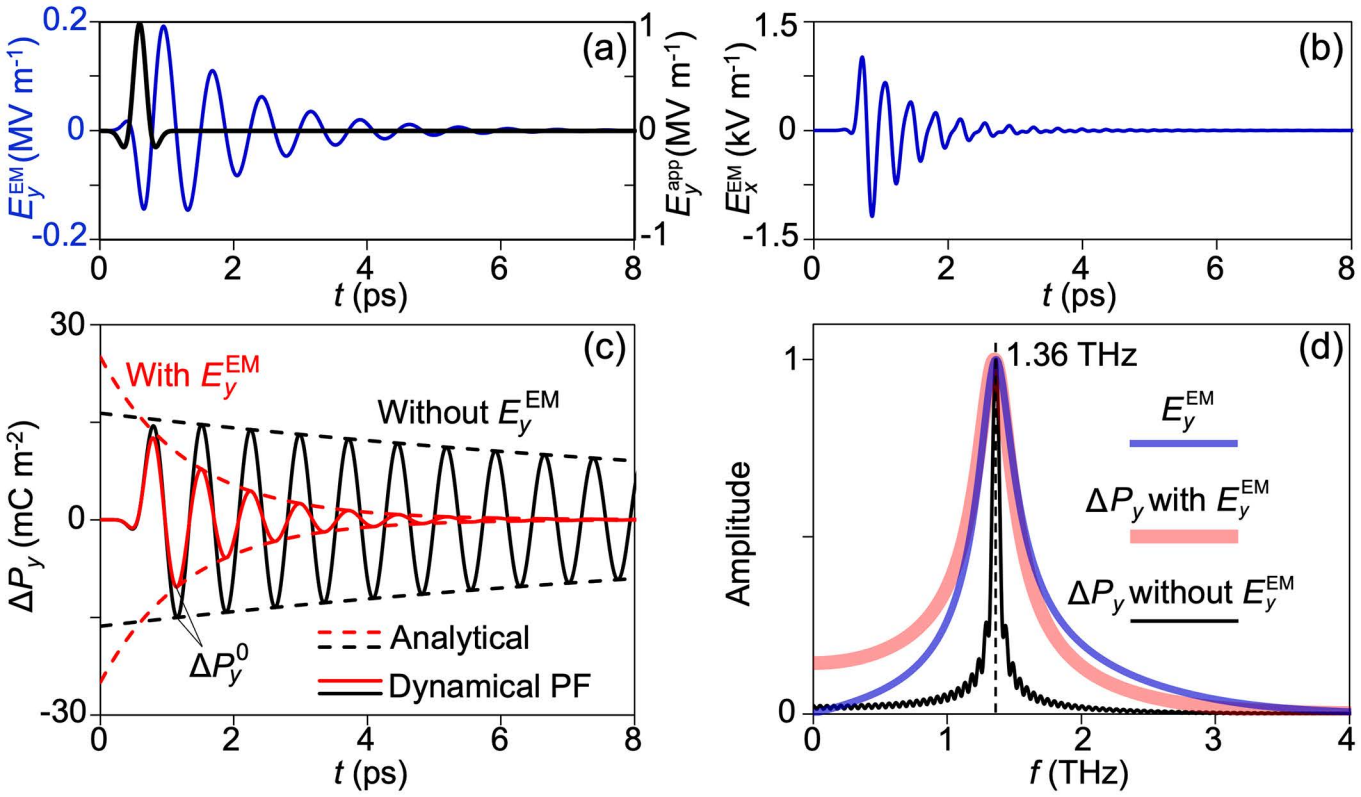
(a)
E_y^{EM} (MV m^{-1})
E_y^{app} (MV m^{-1})
0.2
0
-0.2
1
0
-1
0
2
4
6
8
t (ps)
(b)
E_x^{EM} (kV m^{-1})
1.5
0
-1.5
0
2
4
6
8
t (ps)
(c)
With E_y^{EM}
Without E_y^{EM}
ΔP_y (mC m^{-2})
30
0
-30
ΔP_y^0
Analytical
Dynamical PF
0
2
4
6
8
t (ps)
(d)
1.36 THz
E_y^{EM}
ΔP_y with E_y^{EM}
ΔP_y without E_y^{EM}
Amplitude
1
0
0
1
2
3
4
f (THz)